

X-ray line emissions from tamped thin aluminum targets driven by subpicosecond-duration laser pulses

Peter Hakel^{a,*}, Roberto C. Mancini^a, Ulrich Andiel^b, Klaus Eidmann^b, Francesca Pisani^b, Gwyneth Junkel-Vives^{c,1}, Joseph Abdallah^c

^a Department of Physics, University of Nevada, Reno, NV 89557, USA

^b Max-Planck-Institut für Quantenoptik, Hans-Kopfermann-Str. 1, D-85748, Garching, Germany

^c Theoretical Division, Mailstop B212, Los Alamos National Laboratory, NM 87545, USA

ARTICLE INFO

Article history:

Received 30 July 2007

Received in revised form

16 December 2008

Accepted 16 December 2008

Available online 30 December 2008

PACS:

52.38.-r

52.65.-y

52.25.Os

52.38.Ph

Keywords:

Line emissions

Laser plasmas

Atomic kinetics

ABSTRACT

We report on atomic kinetics and X-ray line spectra modeling work of plasmas generated by high-intensity, ultrashort-duration pulsed lasers. Our work is motivated by the need to analyze and interpret experiments with laser-irradiated layered targets performed at the Max-Planck-Institut für Quantenoptik. The focus of this Paper is on the theoretical characterization of the properties of X-ray line emissions as signatures of plasma conditions. Our model considers several spectral features with detailed attention paid to atomic kinetics, intrinsic spectral lineshapes in a high-density plasma environment (in particular Stark broadening and line shift effects), and spectroscopic-quality radiation transport (opacity effects). We apply our model to the analysis of time-integrated K-shell aluminum X-ray line spectra and time-resolved total line intensities obtained from the layered targets. Modeling calculations indicate that red line shifts observed in these experiments cannot be explained by shifts in the centers of gravity of composite spectral features due to blending with enhanced satellite contributions, but are consistent with intrinsic line shift effects in both resonance and satellite lines. We also investigate the sensitivity of our results to the selection of one of three adopted models for laser-energy deposition and transport within the target.

© 2008 Elsevier B.V. All rights reserved.

1. Introduction

Understanding of the properties and behavior of high-density, high-temperature plasmas is important in the area of Inertial Confinement Fusion (ICF). Formation of high-density, high-temperature plasmas requires systems capable of creating high-energy densities in the studied materials. This can be accomplished by, for example, large laser facilities such as those dedicated to ICF research [1,2]. Another possibility is the use of lower-energy, but shorter (subpicosecond) duration lasers. These are tabletop systems with high-intensity irradiation and high pulse repetition rates that also provide convenient, low-cost opportunities for systematic studies of dense plasmas [3–14].

Plasmas formed by these types of lasers can undergo hydrodynamic expansion during the duration of the laser pulse and line emission can take place during different phases of the target

evolution, which complicates the interpretation and analysis of time-integrated spectra. The plasma can also exhibit strong spatial gradients in temperature and density. These effects can be mitigated by the use of layered targets and isochoric heating of the target by the laser. Instead of irradiating a bulk target, a thin (submicron) layer of a tracer material can be placed on a massive (thickness ~ 1 cm) substrate and then covered by a tamper layer (see Fig. 1). Thus line emission comes from a material whose hydrodynamic expansion is (at least to some extent) arrested by the tamper layer and hence the time history of an approximately uniform plasma can be studied. In our experiments [15–18] the tamper layer is made of carbon and its thickness is 45 nm. The general observed trend is a decrease of satellite line emission and a better observation of resonance lines with the decreasing Al thickness. Also, the tracer layer results lack the small third peak on the Ly- α low-energy wing, that is otherwise visible in the data from the experiment with bulk Al [19]. Line emissions of this type have also been observed in other experiments [20,21] and their origin can be traced to the transitions from triply excited (hollow) Li-like ions. These additional features in the spectra are caused by superpositions of radiation emitted from different portions of the

* Corresponding author. Tel.: +1 775 784 6059; fax: +1 775 784 1398.

E-mail address: phakel@unr.edu (P. Hakel).

¹ Deceased.

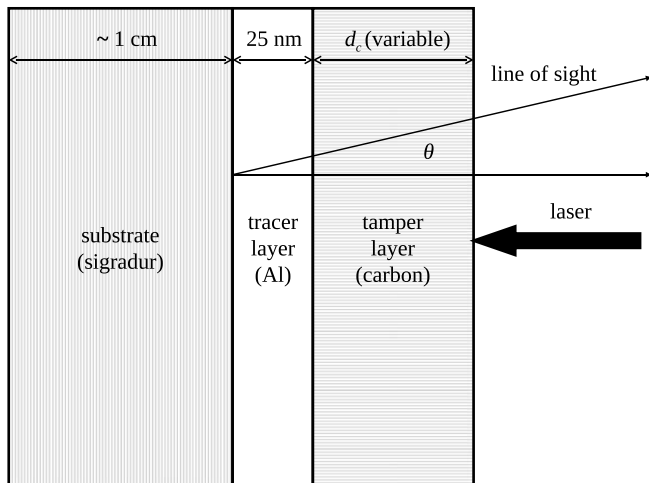


Fig. 1. Schematic of the MPQ layered target with a thin aluminum tracer layer and a carbon tamper layer on a massive sigradur substrate (drawing not to scale).

(inhomogeneous) plasma present in the “bulk” experiment. Time changes of plasma conditions during line emission are also possible. Thus the spectrum from a bulk material is an accumulation of many types of line emissions from different ions. In general, tampered tracer targets of smaller thickness are more uniform in space and thus the spectra they produce are “cleaner” as compared to those from bulk targets. Therefore this experiment suppresses spatial gradients and is thus better suited for our purpose of the modeling and understanding of the properties of hot, dense plasmas. Further aid in modeling of these types of plasmas can be obtained through the use of hydrodynamic codes that model energy deposition in the target and the resulting energy transport and hydrodynamic evolution. In particular, with hydrodynamic simulations one can calculate electron temperature and ion number density time histories in the tracer layer. These can be post-processed by a spectral model that provides level populations and, ultimately, line intensities and spectra.

In this Paper we discuss the elements of the CRAK/SPECTRUM spectral model tailored to study X-ray line emission of hot, dense plasmas. In Sections 2–5 we describe our atomic kinetics model and code CRAK and its particular application to Al plasmas, then we discuss the database of intrinsic emission lineshapes affected by high-density conditions in the plasma, and finally the spectral code SPECTRUM and its role in addressing opacity effects on the emission line spectra. In Sections 6–8 we discuss the application of our model to Al tracer-layer experiments performed with the ultrashort pulse laser ATLAS at the Max-Planck-Institut für Quantenoptik.

2. Collisional-radiative atomic kinetics model and code CRAK

For the purpose of calculating synthetic line spectra recorded in our experiments we have developed a collisional-radiative atomic kinetics model and code CRAK. Time histories of temperature and density needed by CRAK are provided by the hydrocode MULTI-fs [22], which simulates the evolution of plasma conditions in response to the driving laser pulse. CRAK calculates the rates of atomic processes linking ground and singly excited states by analytical formulae that depend on shell labels of valence electrons and absorption oscillator strengths. Collisional excitation rate coefficients are calculated according to [23], rates for ionization follow [24], and radiative recombination rates are based on [25]. Atomic processes considered in CRAK include collisional mixing (excitation and deexcitation) between autoionizing states [26].

These processes are characterized by their respective rates and cross sections.

The free electrons of the plasma are described by a bi-Maxwellian electron distribution function with a low-temperature (T_c) component to model the effect of thermal electrons in the plasma, and a high-temperature (T_h) component to approximate the effect of hot electrons [27]. The hot electron fraction parameter α can assume values between 0 and 1 and characterizes the partition of the electron pool into the thermal and “hot” parts. Typical values of α are of order 0.1 [9,28]. If the total electron number density is N_e , then the number density of hot electrons is αN_e and the number density of the thermal component is $(1 - \alpha)N_e$. The electron distribution function $f(E)$ has the form,

$$f(E) = (1 - \alpha)f_{\text{Maxw}}(T_c, E) + \alpha f_{\text{Maxw}}(T_h, E) \quad (1)$$

where $f_{\text{Maxw}}(T, E)$ is the normalized Maxwellian energy distribution at temperature T . We performed calculations using values for α (~ 0.1 – 0.2) in which we saw no significant effects of the hot electron component on time-integrated spectra. We also point out that the massive sigradur substrate behind the Al layer prevents the hot electrons from coming about and influencing the kinetics later in time. Thus, in the calculations presented below we have chosen $\alpha = 0$.

The CRAK code can also take into account the effects of photoexcitation and photoionization through the use of escape factors for the rates of spontaneous radiative decay and radiative recombination [29]. We find that due to high densities the atomic kinetics is collisionally dominated and opacity effects on level populations are sufficiently accounted for within the escape factor approximation (see Section 4).

In the context of our work on X-ray line emissions from laser-produced Al plasmas the energy level structure and atomic data for CRAK were computed with Cowan’s atomic structure code [30] and Los Alamos atomic structure and scattering codes CATS [31], ACE [32], and GIPPER [33] using the configuration average level of description. A more detailed energy level structure description (LS -term or J -level) is not necessary since at the high plasma densities considered here the population distribution within J -levels and LS -terms is near an LTE distribution [31]. The range of aluminum ions included in the model begins with the Ne-like ion and ends with the fully stripped (FS) ion. Considering the high laser intensities involved in the experiment, we assume that neutral Al atoms, and Al^+ and Al^{2+} ions (Mg- and Na-like Al) are ionized on a very short time scale. These atoms and ions then maintain negligible populations and therefore are not included in our model. The details of energy level structure in each ion are determined by our focus on Ly- α , Ly- β , He- α , He- β , He- γ , and their associated He-, Li-, Be-, and B-like satellites. Only $n = 1$ and $n = 2$ electrons are considered in Ne- through C-like ions. In B- and Be-like ions all configurations with at least one electron in $n = 1$ and no electrons above $n = 3$ are included. The configurations included in Li-like Al are $1s^2 2l$, $1s^2 3l$, $1s^2 4l$, $1s 2l 2l'$, $1s 2l 3l'$, $1s 2l 4l'$, $1s 3l 3l'$, and $1s 3l 4l'$. We do not include triply excited $2l 2l' 2l''$ Li-like (hollow ion) states. These states can reveal their presence via the $2l 2l' 2l'' \rightarrow 1s 2l 2l'$ satellites of $n = 2$ Ly- α satellites. The exclusion of these hollow ion states is consistent with the formation of a thermal ~ 400 eV plasma in a very short time in our experiments. The relevant time scale for the thermalization is the collision time for hot electrons which we estimate as 100 fs from their speed at 20 keV (4×10^9 cm/s) and their requisite range of up to $4 \mu\text{m}$ [34]. In contrast, based on the corresponding cross section [35] the collision time for the creation of holes in the K-shell is much longer: 500 fs. In addition, the decay time due to auto-ionization is rather quick, about 10 fs. Thus the plasma becomes thermal quickly and the generation of Al with holes in the K-shell is not very efficient. This is in agreement with

the experiment which shows only very weak K- α emission for massive Al targets and no K- α emission in the Al tracer-layer spectra. It is noted that in experiments at very high intensity with much more energetic electrons hollow atoms become important and their influence on the ionization balance and the population of excited states has to be taken into account [21].

In the He-like Al ion we consider ground and singly excited states up to $n = 5$, then $2l\ 2l'$, $2l\ 3l'$, $2l\ 4l'$, $3l\ 3l'$, and $3l\ 4l'$. Finally in H-like Al the highest included states are $n = 5$. The total number of energy levels in our model is 271. For this application, the CRAK model operates in a regime of moderate optical depths ($\tau \leq 1$), hence photoexcitation is approximated by escape factors for the Ly- α , Ly- β , He- α , and He- β lines, which were calculated using Stark-broadened lineshapes for the case of slab geometry [29]. Photoionization can also be approximated with escape factors; however, in the cases considered here the opacity effect on this process is negligible. These resonance lines (unlike satellites) are primary candidates for being opaque due to their large absorption oscillator strengths and for having ground states as lower levels.

3. Spectral line profiles

Level populations calculated from CRAK are combined with intrinsic emission line profiles in order to produce synthetic spectra. There are several effects that have influence on the actual lineshapes. These include natural and Doppler broadening [30]; however, in our case the most dominant contribution to intrinsic line profiles comes from high-density effects: Stark broadening and line shift [36–43]. In addition, in dense plasmas free electrons can spend, on average, enough, time inside the orbital volume of electronic clouds, thus partially shielding the nuclear electrostatic pull on the bound electrons. The net result is a red shift of the line [37,40,44].

Thus our model requires another database in addition to atomic data used by CRAK. This database is a collection of intrinsic line profiles for the five resonance lines and their associated satellites. Stark-broadened line profiles have been prepared through the use of MERL multielectron-radiator lineshape code [36,39] and micro-field distribution functions calculated with the APEX model [37,38,41,43] for various combinations of electron number density and temperature. Natural and Doppler broadening effects are also included. In addition, the database also contains information about the dense plasma line shift [44].

We show the importance of the Stark broadening and dense plasma line shift effects on the Ly- α resonance line whose plasma-effects-free intrinsic lineshape is a narrow double-peaked profile due to the fine-structure splitting of the $2p$ upper level into $J = 1/2$ and $3/2$ components. In Figs. 2 and 3 we present the changes in the Ly- α profile for several combinations of electron number density and temperature. In Fig. 2 we observe the suppression of the central dip with increasing electron density. Higher density also results in a more apparent red shift of the line. Fig. 3 reveals a smaller, while still apparent, effect of a changing electron temperature on the Ly- α line. The line shifts depend rather weakly on electron temperature, especially at high temperatures. They increase at lower values of electron temperature since colder electrons can (on average) spend more time inside atomic volumes. The line shift sensitivity on electron density is more significant than its sensitivity to electron temperature [37,44]. In principle, different components of the line can be shifted by different amounts, which could lead to a distortion of the overall spectral feature. In the Ly- α case we observe that the distortion effect of differential line shifts is rather small. Lineshape with more components show more of a distortion effect due to differential line shifts [44].

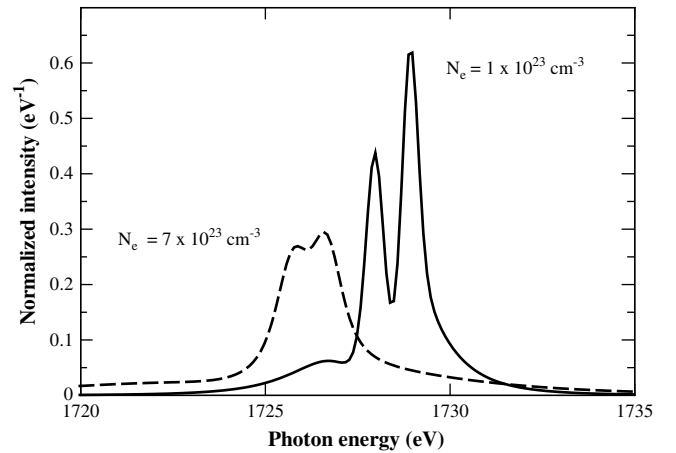


Fig. 2. Variation of the Al Ly- α resonance lineshape with density at electron temperature 300 eV shown for densities $1 \times 10^{23} \text{ cm}^{-3}$ and $7 \times 10^{22} \text{ cm}^{-3}$.

4. Radiation transport

Radiation field arising from the line transition and radiative recombination processes can influence the level populations through radiation-dependent rates such as photoexcitation, photoionization, and stimulated emission. In turn, intrinsic spectral lines profile can differ from the actual lineshapes emerging from plasma. Thus, in the most general case, one needs to solve self-consistently atomic kinetics coupled with the radiation transport equation. The plasmas under our consideration are very dense and therefore this complex task can be simplified. High electron number density means that kinetics is dominated by electron-ion collisions. These conditions allow the use of an approximation, in which atomic kinetics and radiation transport need not be merged into a unified model. Instead, an atomic kinetics model can be evaluated with opacity effects approximated by escape factors, which account for the photoexcitation and photoionization processes by reducing the rates of spontaneous radiative decay and radiative recombination. Escape factors depend on local plasma conditions and the population of the transition's lower level. The resulting fractional populations f_j (and hence ion number densities N_j) can then be post-processed and solved for radiation field I_ν at a given photon energy $h\nu$ via the following (1-D) radiation transport equation [45,46],

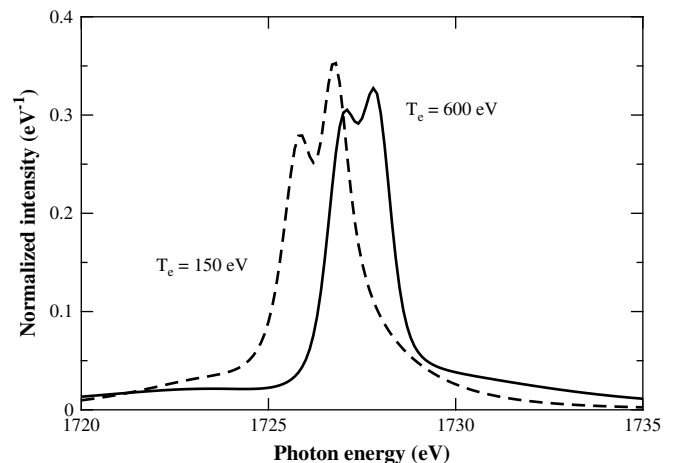


Fig. 3. Variation of the Al Ly- α resonance lineshape with temperature at electron number density $5 \times 10^{23} \text{ cm}^{-3}$ shown for temperatures 150 eV and 600 eV.

$$\cos \theta \frac{dI_\nu(z, \theta)}{dz} = [j_\nu(z) - k_\nu(z)I_\nu(z, \theta)], \quad (2)$$

in which the plasma emissivity j_ν and opacity k_ν are defined as,

$$j_\nu = \sum_i \sum_{j<i} N_i A_{ij} \varphi_{ij,\nu} \frac{h\nu_{ij}}{4\pi}, \quad (3)$$

and

$$k_\nu = \sum_i \sum_{j<i} (N_j B_{ji} - N_i B_{ij}) \varphi_{ij,\nu} \frac{h\nu_{ij}}{4\pi} \quad (4)$$

where θ is the angle between the coordinate axis z and the line of sight (see Fig. 1), A and B are the Einstein coefficients, i and j label the transition's upper and lower levels, and φ_s are normalized emission line profiles (here assumed to be the same as absorption profiles, i.e. we invoke the complete redistribution approximation). In general one expects to see the strongest opacity effect in the α resonance lines, followed by the β resonance lines, while the satellites typically remain optically thin. This expected trend is confirmed by our calculations.

Thus, given the goal of X-ray line spectra modeling, we complement CRAK with the spectral code SPECTRUM, which post-processes CRAK energy level populations. SPECTRUM uses these populations to weigh normalized intrinsic Stark-broadened and shifted lineshapes and solves Equation (2) yielding synthetic spectra with spectroscopic-quality treatment of opacity effects.

5. Model CRAK calculations for layered aluminum targets

In order to illustrate the features of our spectral model in this Section we present the results of steady-state model calculations for two combinations of a single temperature and electron number densities for the types of targets used in experiments (see Fig. 1). We focus on two spectral features: 1) the Ly- α (the resonance line and its $n = 2, 3, 4$ He-like satellites), and, 2) the He- β (the resonance line and its $n = 2, 3, 4$ Li-like satellites). To this end we selected the temperature of 200 eV and two electron number density values: 1×10^{22} and 2×10^{23} el./cm³. These two densities roughly mark the low end and the mid-range of the general regime expected in the experiments discussed later in this paper. The chosen temperature is sufficiently high to put a significant amount of ion population in the He- and H-like Al ions from which these two spectral features originate.

The spectra in Figs. 4–7 were calculated in the optically thin approximation for an Al slab of 25 nm thickness. In this

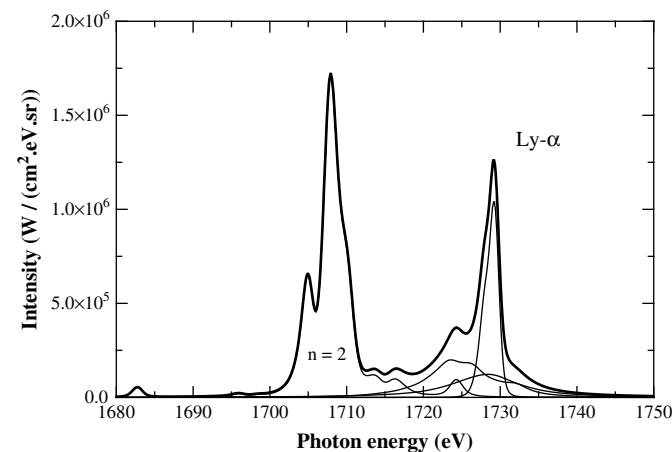


Fig. 4. Intrinsic lineshape of the Ly- α spectral feature in the optically thin approximation (Al slab thickness 25 nm). $T = 200$ eV, $N_e = 1 \times 10^{22}$ el./cm³.

approximation the total spectrum is a simple sum of all the components present in the model. At the lower density we observe a rich line structure coming from the satellites on the red wings of both resonance lines. At the higher density all the lines become strongly broadened by the Stark effect and the overall spectral profile becomes deceptively simple in appearance. Nevertheless, the importance of inclusion of satellite lines (even though they no longer contribute with their multiple-peaked lineshapes) is particularly apparent in Fig. 7. While the $n = 3$ and 4 satellite contributions are very broad and therefore do not qualitatively alter the line profile coming from the resonance line, they are strong enough to significantly enhance the intensity of the overall He- β spectral feature. Therefore, preserving the completeness of a spectral model even at these high densities is necessary, especially if line intensities are to be used to infer the temperature.

6. MPQ Al tracer-layer experiments

The ATLAS Ti:Sapphire laser of the Max-Planck-Institut für Quantenoptik (MPQ) [47] can deliver approximately 70 mJ at (frequency doubled) $\lambda = 395$ nm in a pulse of FWHM of 150 fs. The intensity is about 6×10^{17} W/cm² and the laser is focused to spots approximately 10 μ m in diameter. The contrast ratio is 10^{-10} in the temporal window between 30 and 2 ns before the main pulse and better than 10^{-6} at 1 ps before the maximum of the main pulse. The angle of incidence on the target may be in the range of 30–80° with s- or p-polarization in order to maximize the absorption of laser energy. The measurements presented here were performed with p-polarized laser light at an angle of incidence of 45°. As is schematically shown in Fig. 1, the targets consisted of a flat sigradur (a glasslike carbon modification) plate which was covered by a 25 nm thick Al layer and carbon tamper layers of thicknesses 25 nm, 50 nm, 100 nm, 200 nm, and 400 nm. The main advantage of using carbon instead of MgO employed in earlier experiments [48] is the elimination of magnesium lines in the 1.7–1.9 keV range that overlap with the H- and He-like Al emissions of interest. The spectra were measured by crystal spectrometers as time-integrated as well as time-resolved. More details of the experiment are given in references [15–17,49]

In order to model the plasma behavior in these experiments, we used the atomic kinetics code CRAK to post-process time histories of electron temperature and ion number density computed with a hydrodynamic code. In a first attempt we used MULTI-fs [22] for this purpose. This is the short-pulse version of the original (ns-pulse) MULTI one-dimensional Lagrangian hydrocode based on a one-fluid two-temperature model including electronic heat

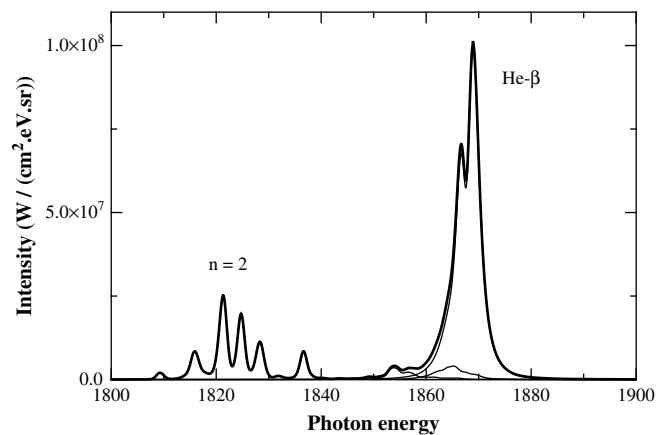


Fig. 5. Intrinsic lineshape of the He- β spectral feature in the optically thin approximation (Al slab thickness 25 nm). $T = 200$ eV, $N_e = 1 \times 10^{22}$ el./cm³.

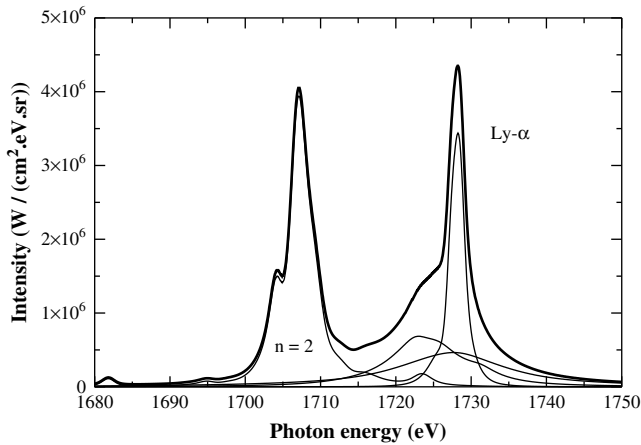


Fig. 6. Intrinsic lineshape of the Ly- α spectral feature in the optically thin approximation (Al slab thickness 25 nm). $T = 200$ eV, $N_e = 2 \times 10^{23}$ el./cm 3 .

conduction, multigroup radiation transport, and SESAME equation of state [50]. Essential modifications for the treatment of ultra-short-duration pulses in this hydrocode are the solution of Maxwell's equations in a steep-gradient plasma within the skin depth, consideration of the non-equilibrium between electrons and ions, and a model for the electrical and thermal conductivity covering the wide range from solid state to high-temperature plasma.

MULTI-fs predicts at the oblique 45° incidence of p-polarized light an effective absorption of about 50% in agreement with the experiment [51]. The absorbed energy creates a very hot thin front layer of several 10 keV, and within the Spitzer's heat flow approximation used by MULTI-fs, a heat wave with a steep temperature front propagates into the solid target. However, this approximation is no longer valid, because the mean free path of the hot electrons exceeds considerably the thickness of the heat wave. Indeed, spectra calculated by post-processing time histories generated with standard Spitzer heat flow implemented in MULTI-fs, showed a strong excess of H-like line emission for thin tamper layers and a strong excess of He-like emission at thick tamper layers, in contradiction to the experiment. More realistic time histories were obtained by assuming that the hot electrons propagate into the target by typical distances given by their mean free path. For the spatial profile of energy deposition we used several models. In previous calculations [16,17] we made an *ad hoc* assumption by using a uniform energy deposition up to the mean free path of the

electrons. This was motivated by the fact, that the line ratios in the measured spectra (in particular the intensity ratio of Ly- β and He- β) did not change with the tamper layer thickness, which indicates a constant temperature for the depths studied. In the calculations presented below we use a more rigorous model for the energy deposition.

7. Post-processing of MULTI-fs temperature and density time histories with CRAK

In the hydrodynamic simulations the thin Al layer is represented by several fluid elements, of which we have used the mass-weighted averaged time histories of electron temperature and ion number density as representatives for the entire Al slab. This is justified by the achieved high degree of uniformity in the 25-nm thick tracer layer as indicated by the MULTI-fs simulations, especially for the cases with thicker tamper layers. The results of MULTI-fs simulations are given in Figs. 8 and 9.

The typical behavior of the temperature (Fig. 8) is a rapid increase during the heating phase of the first 300 fs followed by a slower cooling due to heat conduction and expansion. The temperatures for the depths up to 200 nm are very similar. This feature was obtained in previous calculations [17] in an *ad hoc* way to model the heat transport via energetic electrons by using a uniform energy deposition up to the hot electrons' range. This was motivated by the fact, that the line ratios in the measured spectra (in particular the intensity ratio of Ly- β and He- β) did not change with the tamper layer thickness, which indicates a constant temperature for the depths studied. It is noted, that for depths larger than about 1000 nm the temperature derived from spectra in layered targets decreases in agreement with the range expected for 20 keV electrons [18]. In the results presented here the uniform temperature for the considered range of tamper thicknesses was obtained from an alternative model [52]. It was assumed that an electron flow with an intensity of 2.5×10^{17} W/cm 2 and a Maxwellian distribution with a temperature of 20 keV enters the target during the interval when the laser pulse interacts with the target. This intensity corresponds to the absorbed flux due to resonance absorption [51] and reproduces the measured ratio of the Ly- β and He- β intensities. The temperature of 20 keV has been concluded from the measurement of the Bremsstrahlung continuum [15,16].

The clearest trend in the time history of the ion number density is the halt of the initial decompression of the tracer layer behind the tamper layer, which is increasingly evident for the thicker tamper

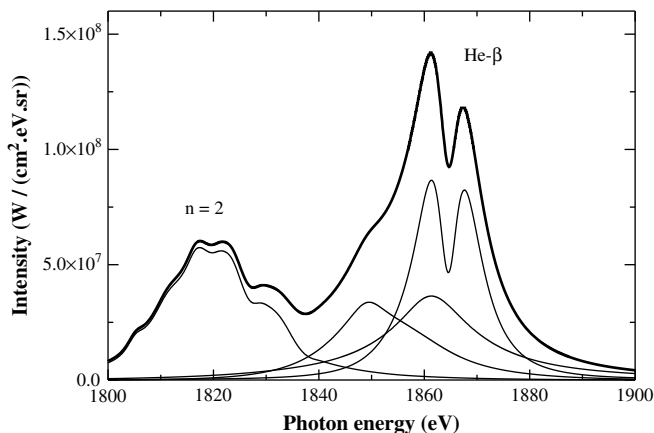


Fig. 7. Intrinsic lineshape of the He- β spectral feature in the optically thin approximation (Al slab thickness 25 nm). $T = 200$ eV, $N_e = 2 \times 10^{23}$ el./cm 3 .

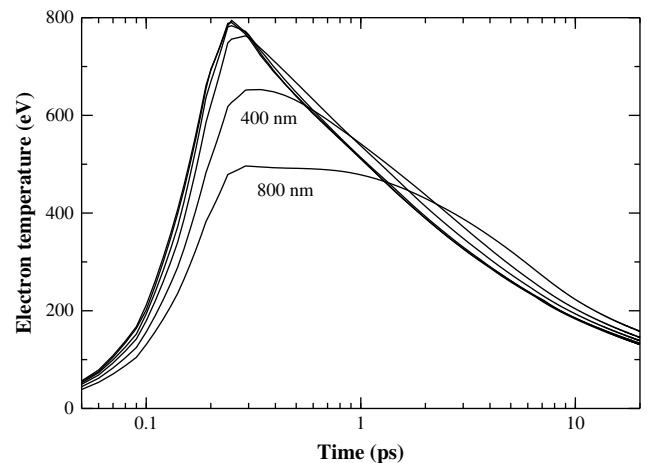


Fig. 8. Temperature evolution according to MULTI-fs hydrodynamic simulations for Al slabs of 25 nm thickness under carbon tamper layers of 25, 50, 100, 200, 400, and 800 nm thickness.

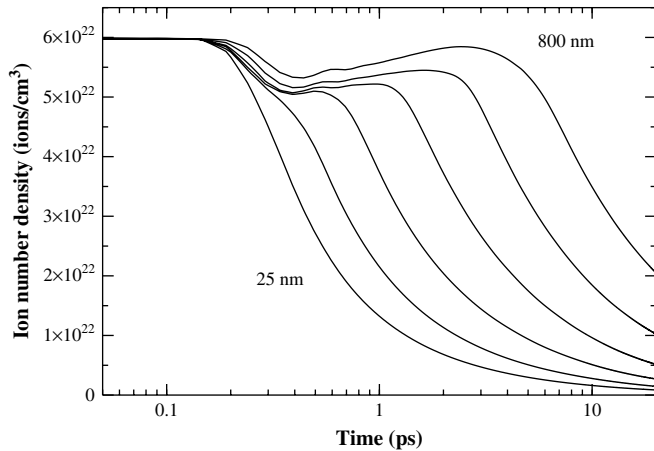


Fig. 9. Ion number density evolution according to MULTI-fs hydrodynamics simulation for Al slabs of 25 nm thickness under carbon tamper layers of 25, 50, 100, 200, 400, and 800 nm thickness.

layers. The initial decompression is caused by the rapid expansion of the Al of mass density 2.7 g/cm^3 into the solid carbon of slightly lower mass density (2.3 g/cm^3). After this early decompression the Al sample layer stays for a while at high density. Later on a slower expansion sets in that proceeds faster when the aluminum slab has less carbon to push in front of it. In addition, the cases with the thicker tamper layers above 100 nm indicate the presence of another, milder compression caused by a shock wave evolving in the target.

These MULTI-fs simulation results were post-processed with CRAK running in the fully time-dependent mode with escape factors included for Lyman and Helium α and β lines.² In this transient, high-density regime dominated by electron–ion collisions, opacity effects are found to have negligible impact on the kinetics but they significantly affect the line intensity distribution. As a consequence of their very short lifetime, the direct effect of the penetrating hot electrons on the spectra through kinetics is negligible. They affect the spectra only indirectly, by increasing the “cold” (thermal) electron temperature up to a certain target depth. Therefore we model the effect of the hot electrons on the kinetics by assuming that their temperature profile peaks at, alternatively, 8 and 20 keV with negligible differences in the resulting synthetic spectra. As a function of time, in CRAK the effective hot electron temperature follows the temporal intensity profile of the laser pulse, which is a Gaussian centered at 300 fs with FWHM of 150 fs. The shortness of the duration of the hot electrons follows from the short collision time of electrons with the cold target mentioned in Section 1 and also from the subpicosecond electron–electron collision time for 20 keV electrons. Furthermore, since their velocity is about $0.2c$, these electrons will reach the depth of up to 1000 nm, where the tracer layers are located, within a short time of less than 20 fs. Having passed through these front layers the hot electrons thermalize in deeper target regions. This is confirmed by Propel [53] electron kinetic calculations which showed only a very small amount of backscattered electrons. Our thick target situation is different from thin foil experiments where the electrons are reflected at the rear surface and trapped in the foil. For these reasons we assume that the heating time and hot electron presence does not considerably exceed the laser pulse duration. Thus, the

results presented below were calculated without the direct effect of fast electrons on atomic kinetics and level populations.

Fig. 10 shows examples of average ionization time histories. In this Figure the two phases in plasma evolution – the ionization and recombination phases – are clearly visible. Approximately at the time $t = 1 \text{ ps}$ the plasma begins a partial recombination phase. Note that this time is later than the time of maximum temperature (about 300 fs, see Fig. 8). This shows that a fully time-dependent treatment is important. In steady state the maximum ionization would be expected at the time of the temperature maximum (see Fig. 10). Fig. 11 shows the synthetic spectra for all six tamper layer thicknesses. More heavily tamped Al layers experience higher electron densities for longer periods of time, which translates into broader line profiles. In Fig. 12 we present detailed comparisons of synthetic spectra calculated using the three energy-deposition models available in the MULTI-fs hydrocode: uniform deposition [17], the Harrach–Kidder model [52], and a Monte Carlo model named Propel [53]. This allowed us to test the sensitivity of the time-integrated synthetic spectra to the details of three independent energy-deposition models. The differences between the three models are small for the thin tampers but grow larger with the increasing tamper thickness. This is indicative of the gradual divergence of the three used energy-deposition models with the increasing depth. In particular, for thinner tampers the Ly- β line is stronger in the Monte Carlo (Propel) calculation than in the other two models, this trend is notably reversed at 400 nm. This is consistent with the notion that the energy carriers (hot electrons) stop being effective at about this depth according to the Propel model. Naturally, with the assumption of uniform energy deposition the Ly- β remains strong regardless of tamper thickness.

Finally in Fig. 13 we present comparisons of our calculated results with experimental data. In these plots, a continuum bremsstrahlung emission of $T = 250 \text{ eV}$ originating from the fully ionized carbon was added and the line spectrum (which is calculated in absolute units) was rescaled by a factor of order unity to account for the uncertainty in the focal spot size. The agreement between the theory and the experiment is generally good, including the He- δ line ($\sim 2000 \text{ eV}$) at 25 nm thickness which was not included in the original model [48] because in all other cases it is too broad to be visible in the measurement. We have consistently observed that the most intense ($n = 2$) satellites of the Ly- α remain well separated from their parent line without changing the distance to the parent line. In other words, the Ly- α line together with its He-like satellite shows an increasing “block-shift” with the

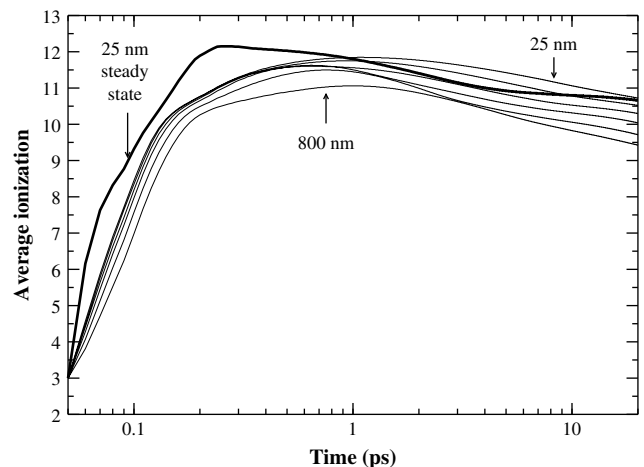


Fig. 10. Time evolution of average ionization (\bar{z}) obtained from CRAK post-processing of MULTI-fs results from Figs. 8 and 9.

² The runtimes for both the CRAK and SPECTRUM codes for one time history are in the order of a few minutes on a 3 GHz Intel Xeon Linux PC when compiled and optimized with the Intel Fortran 90 compiler.

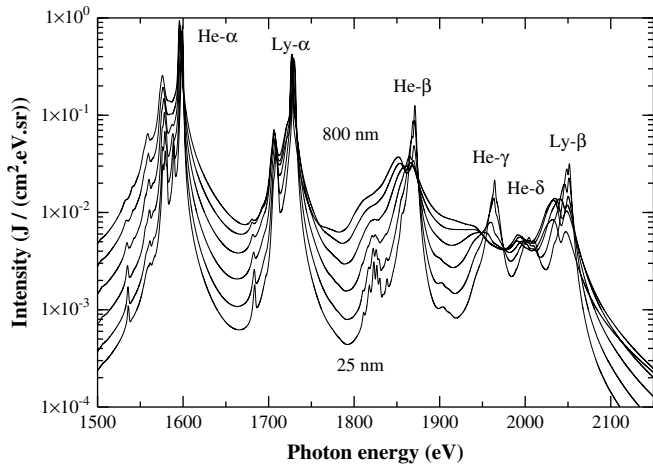


Fig. 11. Time-integrated synthetic spectra for the six tamper thicknesses calculated by spectral post-processing of CRAK level population results, with the inclusion of opacity effects.

depth of the tracer layer, i.e. with density, see Fig. 1 in [17]. Higher satellites ($n > 2$) are weaker and progressively Stark-broadened to the point that they either mildly distort the red wing of the parent line or slightly lift the entire spectral feature without any discernible effect on the resonance line’s shape or position. Some differences appear in the Ly- β feature and the satellites of He- α , which are both less intense in the model as compared to the experiment. The underestimation of the Ly- β would suggest the need for higher effective temperatures driving more emission from H-like ions, while the stronger than calculated He- α satellites lead to considering lower temperatures. This apparent contradiction can be addressed by considering that the synthetic spectra were calculated assuming a simple 1-D geometry, i.e. a uniform laser focal spot. This is indeed an oversimplification; the experimental spectra are spatially integrated along the line of sight which cuts across regions with different plasma conditions pursuant to the local laser intensity. The subsequent time integration of emissions from these various parts of the plasma further complicates the analysis. Therefore, the most natural improvement of our model would be to “overlay” several versions of our spectral model (with properly upgraded solution of the radiation transport equation), each driven by its own laser intensity characteristics. An independent

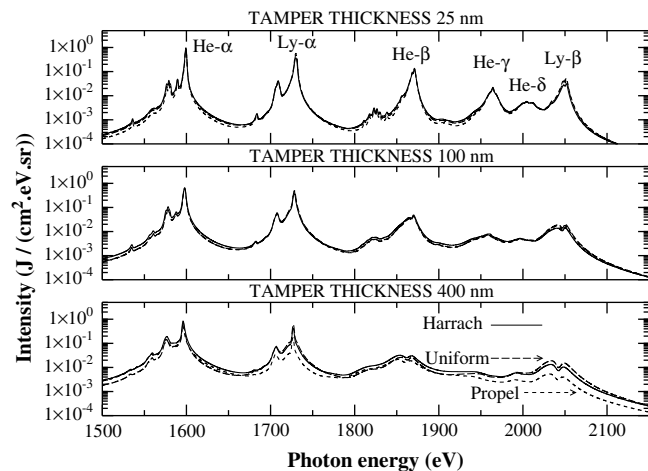


Fig. 12. Comparisons of synthetic time-integrated spectra obtained from the three studied energy-deposition models.

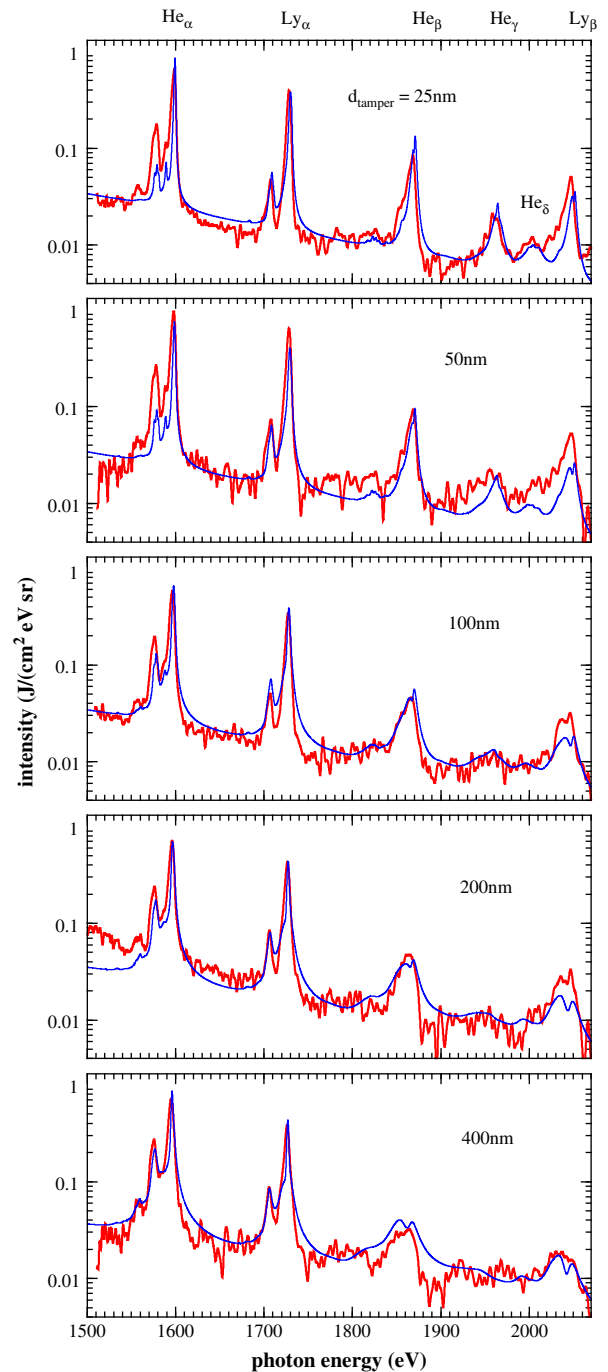


Fig. 13. Comparisons of synthetic time-integrated spectra obtained using the Harrach-Kidder energy-deposition model with experimental measurements for several tamper thicknesses.

measurement of the shape and intensity distribution of the laser focal spot size would greatly aid such an improvement in modeling capability.

The calculated spectra shown in the previous Figures were obtained by integrating the radiation during the whole time interval of emission. Because the consideration of the time dependence is a basic feature of the model, we show now some time-resolved results for the emitted radiation. In Fig. 14 we have plotted the time dependence of the Ly- α and He- α lines along with their satellites which are emitted from the 25 nm Al sample layer, when the carbon tamper thickness was 200 nm. In the calculation

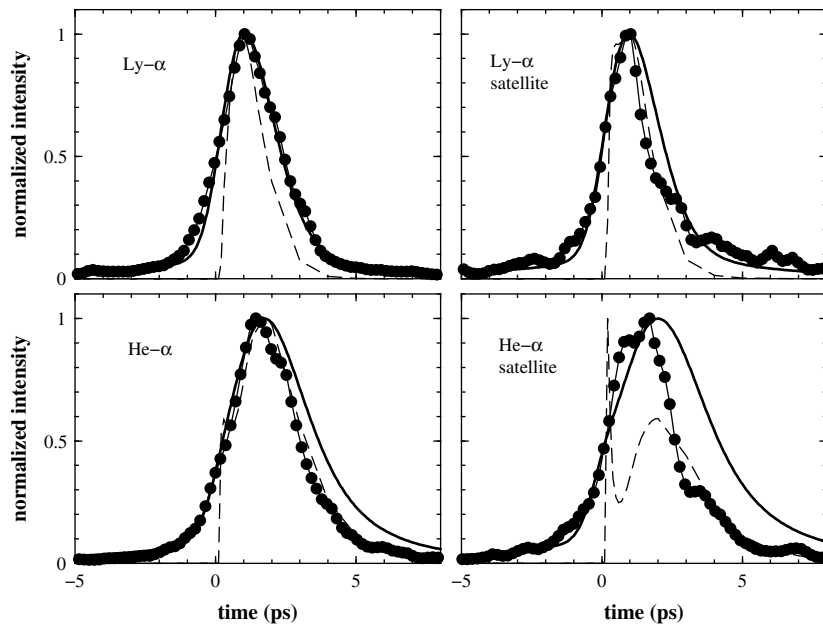


Fig. 14. Time dependence of the Ly- α and He- α lines and their satellites emitted by the 25 nm Al sample layer under a 200 nm thick carbon tamper. The measurements (filled circles) are compared with the raw calculated results (dashed lines) and the calculated results folded with the temporal resolution of the measurement (solid line).

(the dashed curve) one observes a rapid increase of the emission at a time when the temperature reaches the maximum (at about $t = 300$ fs, see Fig. 13). The emission increases further and reaches a maximum at around 1 ps, which corresponds to the time of maximum ionization (see Fig. 8). After that the emission decays during a few ps. The time dependence of the He-like lines is somewhat more complicated. In particular, the He- α satellite shows a short initial spike and after that a second maximum. This is attributed to the ionization which reaches quickly He-like populations and changes then to H-like population causing the minimum. Later on during the cooling phase again He-like states are populated causing the second maximum. For comparison with the experiment we have folded the theoretical result with the experimental time-resolution (about 1 ps) yielding the solid curves. The overall agreement with the measurement supports the validity of the model. Finally we note that our model is also confirmed by the agreement of the measured red line shifts with the model. This point has been discussed in detail in [17].

8. Discussion and conclusions

We have modeled and discussed the measured X-ray spectra generated by subpicosecond-duration laser pulses irradiating solid thin Al layered targets covered by tamper layers of varying thicknesses. Model calculations were based on post-processing temperature and density time histories from hydrodynamic simulations with a detailed atomic and radiation physics model. We performed hydrodynamic simulations with several models of laser-energy deposition and transport by non-thermal electrons, which were then post-processed by a time-dependent collisional-radiative atomic kinetics model with a self-consistent account of auto-ionizing states. Synthetic spectra were then generated with opacity effects taken into consideration. Overall we have obtained good agreement between the model and the time-integrated experimental data from a wide wavelength range, simultaneously considering Al He- α , β , γ and δ , and Ly- α and Ly- β features, and their associated satellite lines. Furthermore, the satisfactory comparison of the time-resolved total line emissions from He- α , Ly- α and their

satellites provides an additional argument for the validity of the CRAK approach. It shows that our model provides a sufficient understanding of both resonance and satellite line formation and therefore allows us to rule out satellite line emissions as the cause of observed resonance line shifts. Our observations of line broadening indicate that electron densities remain at high values for longer time intervals when thicker tamper layers are used. The observed lack of sensitivity of line intensities to the tamper thickness is a signature of energetic electrons penetrating the target deeper than would be expected in a regime of diffusive energy deposition. In addition, a precise experimental wavelength calibration employed in these experiments [16–18], enabled a detailed modeling study of the effect of dense plasma line shifts both in resonance and satellite lines. We note that the absence of such shifts in other experiments [54,55] can be due to their different experimental conditions in which the thin Al layers were either free-standing or coated by carbon on only one side. Unlike in our case with Al covered on both sides, arrangements of these experiments allowed the plasma to expand much faster resulting in lower typical densities thus reducing the line shift effect. Line shifts have in fact been observed in other experiments with free-standing Al foils [56]. There, higher densities were likely achieved through the use of thicker targets (up to 5 μm). The careful account of satellite line transitions in our model allows us to conclude that the red line shifts observed in our experiments cannot be explained as a distortion of the (unshifted) resonance lines due to blending with their satellites. Instead, detailed lineshape calculations including dense plasma line shifts must be performed if the synthetic spectral line positions are to be reconciled with precisely wavelength-calibrated experimental lines. Finally, further improvement in modeling is suggested by considering the possible non-uniformity of the laser focal spot.

Acknowledgements

This work was supported by the Lawrence Livermore National Laboratory contract B503614, NATO grant CRG 971588, and the Max-Planck-Gesellschaft. We also gratefully acknowledge support

from the University and Community College System of Nevada during the research and (P.H.) from Los Alamos National Laboratory and Rutherford Appleton Laboratory during the finalization of this publication.

References

- [1] J.D. Kilkenny, R.W. Lee, M.H. Key, J.G. Lunney, *Phys. Rev. A* 22 (6) (1980) 2746.
- [2] C.J. Keane, R.W. Lee, B.A. Hammel, A.L. Osterheld, L.J. Suter, A. Calisti, F. Khelifaoui, R. Stamm, B. Talin, *Rev. Sci. Instrum.* 61 (10) (1990) 2780.
- [3] J.C. Kieffer, J.P. Matte, M. Chaker, Y. Beaudoin, C.Y. Chien, S. Coe, G. Mourou, J. Dubau, M.K. Inal, *Phys. Rev. E* 48 (6) (1993) 4648.
- [4] O. Peyrusse, J.C. Kieffer, C.Y. Côté, M. Chaker, *J. Phys. B* 26 (1993) L511.
- [5] D. Umstadter, X. Liu, J. Workman, *Proc. SPIE-Int. Soc. Opt. Eng. (USA)* 1860 (1993) 80.
- [6] D. Umstadter, J. Workman, A. Maksimchuk, X. Liu, U. Ellenberger, J.S. Coe, C.Y. Chien, *J. Quant. Spectrosc. Radiat. Transfer* 54 (1–2) (1995) 401.
- [7] J.P. Matte, J.C. Kieffer, S. Ethier, M. Chaker, O. Peyrusse, *Phys. Rev. Lett.* 72 (8) (1994) 1208.
- [8] R.C. Mancini, P. Audebert, J.P. Geindre, A. Rousse, F. Falliès, J.C. Gauthier, A. Mysyrowicz, J.P. Chambaret, A. Antonetti, *J. Phys. B* 27 (9) (1994) 1671.
- [9] R.C. Mancini, A.S. Shlyaptseva, P. Audebert, J.P. Geindre, S. Bastiani, J.C. Gauthier, G. Grillon, A. Mysyrowicz, A. Antonetti, *Phys. Rev. E* 54 (4) (1996) 4147.
- [10] A. Rousse, P. Audebert, J.P. Geindre, F. Falliès, J.C. Gauthier, A. Mysyrowicz, G. Grillon, A. Antonetti, *Phys. Rev. E* 50 (3) (1994) 2200.
- [11] Z. Jiang, J.C. Kieffer, J.P. Matte, M. Chaker, O. Peyrusse, D. Gilles, G. Korn, A. Maksimchuk, S. Coe, G. Mourou, *Phys. Plasmas* 2 (5) (1995) 1702.
- [12] U. Teubner, P. Gibbon, E. Förster, F. Falliès, P. Audebert, J.P. Geindre, J.C. Gauthier, *Phys. Plasmas* 3 (7) (1996) 2679.
- [13] C.Y. Côté, J.C. Kieffer, O. Peyrusse, *Phys. Rev. E* 56 (1) (1997) 992.
- [14] J.-C. Gauthier, J.P. Geindre, P. Audebert, S. Bastiani, C. Quoix, G. Grillon, A. Mysyrowicz, A. Antonetti, R.C. Mancini, *Phys. Plasmas* 4 (5) (1997) 1811.
- [15] U. Andiel, Isochore Heizung von festem Aluminium mit Femtosekunden-Laserpulsen: eine röntgenspektroskopische Untersuchung der K-Schalene-mission, Dissertation, Technische Universität München, 2001.
- [16] K. Eidmann, U. Andiel, F. Pisani, P. Hakel, R.C. Mancini, G.C. Junkel-Vives, J. Abdallah, K. Witte, *J. Quant. Spectrosc. Radiat. Transfer* 81 (2003) 133.
- [17] U. Andiel, K. Eidmann, P. Hakel, R.C. Mancini, G.C. Junkel-Vives, J. Abdallah, K. Witte, *Europhys. Lett.* 60 (6) (2002) 861–867.
- [18] K. Eidmann, U. Andiel, F. Pisani, P. Hakel, R.C. Mancini, J. Abdallah, G.C. Junkel-Vives, K. Witte, X-ray spectroscopy of dense plasmas produced by isochoric heating with ultrashort laser pulses, in: J.S. Cohen, S.F. Mazevet, D.P. Kilcrease (Eds.), *AIP Conference Proceedings 730, Atomic Processes in Plasmas*, 2004, p. 81.
- [19] K. Eidmann, U. Andiel, E. Förster, I.E. Golovkin, R.C. Mancini, R. Rix, A. Saemann, T. Schlegel, I. Uschmann, K. Witte, Spectroscopy of plasmas at solid density generated by ultrashort laser pulses, in: R.C. Mancini, R.A. Phaneuf (Eds.), *AIP Conference Proceedings 547, Atomic Processes in Plasmas*, 2000, p. 238.
- [20] A.M. Urnov, J. Dubau, A.Ya. Faenov, T.A. Pikuz, I.Yu. Skobelev, J. Abdallah, R.E.H. Clark, J. Cohen, R.P. Johnson, G.A. Kyrala, M.D. Wilke, A.L. Osterheld, *JETP Lett.* 67 (7) (1998) 489.
- [21] F.B. Rosmej, A.Ya. Faenov, T.A. Pikuz, A.I. Magunov, I.Yu. Skobelev, T. Augustine, P. D'Oliveira, S. Hulin, P. Monot, N.E. Andreev, M.V. Chegotov, M.E. Veisman, *J. Phys. B* 32 (5) (1999) L107.
- [22] K. Eidmann, J. Meyer-ter-Vehn, T. Schlegel, S. Hüller, *Phys. Rev. E* 62 (1) (2000) 1202.
- [23] R. Mewe, *Astron. Astrophys.* 20 (2) (1972) 215.
- [24] W. Lotz, *Z. Phys. A* 220 (5) (1969) 466.
- [25] M.J. Seaton, *Mon. Not. R. Astron. Soc.* 119 (2) (1959) 81.
- [26] V.L. Jacobs, M. Blaha, *Phys. Rev. A* 21 (2) (1980) 525.
- [27] R. Epstein, S. Skupsky, J. Delettrez, *J. Quant. Spectrosc. Radiat. Transfer* 35 (2) (1986) 131.
- [28] B. Soom, H. Chen, Y. Fisher, D.D. Meyerhofer, *J. Appl. Phys.* 74 (9) (1993) 5372.
- [29] R.C. Mancini, R.F. Joyce, C.F. Hooper Jr., *J. Phys. B* 20 (1987) 2975.
- [30] R.D. Cowan, *The Theory of Atomic Structure and Spectra*, University of California Press, 1981.
- [31] J. Abdallah Jr., R.E.H. Clark, R.D. Cowan, Los Alamos National Laboratory Report LA-11436-M, vol. I, 1988.
- [32] R.E.H. Clark, J. Abdallah Jr., G. Csanak, J.B. Mann, R.D. Cowan, Los Alamos National Laboratory Report LA-11436-M, vol. II, 1988.
- [33] R.E.H. Clark, J.B. Mann, G. Csanak, A.L. Merts, Los Alamos National Laboratory Report LA-UR-89-2675, vol. 2, 1989.
- [34] M.J. Berger, S.M. Seltzer, Tables of energy losses and ranges of electrons and positrons, in: Nuclear Science Series, Report Number 39, Publication 1133, National Academy of Sciences-National Research Council, Washington, D.C., 1964 p. 205.
- [35] X. Long, M. Liu, F. Ho, X. Peng, *At. Data Nucl. Data Tables* 45 (2) (1990) 353.
- [36] R.C. Mancini, D.P. Kilcrease, L.A. Woltz, C.F. Hooper Jr., *Comput. Phys. Commun.* 63 (1991) 314.
- [37] H. Nguyen, M. Koenig, D. Benredjem, M. Caby, G. Coulaud, *Phys. Rev. A* 33 (2) (1986) 1279.
- [38] M. Koenig, P. Malnoul, H. Nguyen, *Phys. Rev. A* 38 (4) (1988) 2089.
- [39] L.A. Woltz, C.F. Hooper Jr., *Phys. Rev. A* 38 (9) (1988) 4766.
- [40] H.R. Griem, M. Blaha, P.C. Kepple, *Phys. Rev. A* 41 (10) (1990) 5600.
- [41] C.A. Iglesias, H.E. DeWitt, J.L. Lebowitz, D. MacGowan, W.B. Hubbard, *Phys. Rev. A* 31 (3) (1985) 1698.
- [42] A. Calisti, F. Khelifaoui, R. Stamm, B. Talin, R.W. Lee, *Phys. Rev. A* 42 (9) (1990) 5433.
- [43] D.P. Kilcrease, *J. Quant. Spectrosc. Radiat. Transfer* 51 (1–2) (1994) 161.
- [44] G.C. Junkel, M.A. Gunderson, C.F. Hooper Jr., D.A. Haynes Jr., *Phys. Rev. E* 62 (4) (2000) 5584.
- [45] D.P. Mihalas, *Stellar Atmospheres*, second ed. Freeman, 1978.
- [46] R.J. Rutten, *Radiative Transfer in Stellar Atmospheres*, lecture notes Utrecht University 8th WWW edition. Available from: <http://www.fys.ruu.nl/%7Erutten/education/rjr-material/rtsa/afy.pdf>.
- [47] H. Baumhacker, A. Bösward, H. Haas, K.J. Witte, U. Andiel, J. Bayerl, X. Dong, M. Dreher, K. Eidmann, M. Fischer, M. Hegelich, M. Kaluza, S. Karsch, G. Pretzler, H. Stehbeck, G. Tsakiris, *Advanced Titanium Sapphire Laser ATLAS volume MPQ-272 of Laboratory report, Max-Planck-Institut für Quantenoptik*, 2002.
- [48] A. Saemann, K. Eidmann, I.E. Golovkin, R.C. Mancini, E. Anderson, E. Förster, K. Witte, *Phys. Rev. Lett.* 82 (24) (1999) 4843.
- [49] U. Andiel, K. Eidmann, F. Pisani, K. Witte, I. Uschmann, O. Wehrhan, E. Förster, *Rev. Sci. Instrum.* 74 (2003) 2369.
- [50] R. Ramis, R. Schmalz, J. Meyer-ter-Vehn, *Comput. Phys. Commun.* 49 (3) (1988) 475.
- [51] K. Eidmann, R. Rix, T. Schlegel, K. Witte, *Europhys. Lett.* 55 (2001) 334.
- [52] R.J. Harrach, R.E. Kidder, *Phys. Rev. A* 23 (2) (1981) 887.
- [53] T. Schlegel, S. Bastiani, L. Grémillet, J.-P. Geindre, P. Audebert, J.C. Gauthier, E. Lefebvre, G. Bonnaud, J. Delettrez, *Phys. Rev. E* 60 (1999) 2209.
- [54] P. Audebert, R. Shepherd, K.B. Fournier, O. Peyrusse, D. Price, R. Lee, P. Springer, J.-C. Gauthier, L. Klein, *Phys. Rev. Lett.* 89 (26) (2002) 265001.
- [55] R. Shepherd, P. Audebert, K. H-Chen, K.B. Fournier, O. Peyrusse, S. Moon, R.W. Lee, D. Price, L. Klein, J.C. Gauthier, P. Springer, *J. Quant. Spectrosc. Radiat. Transfer* 81 (2003) 431.
- [56] O. Renner, J. Limpouch, E. Krousky, I. Uschmann, E. Förster, *J. Quant. Spectrosc. Radiat. Transfer* 81 (2003) 385.